Electronic Supplementary Material (ESI) for Nanoscale.

Supporting information

Mechanisms behind the enhancement of thermal properties of graphene nanofluids

M. R. Rodríguez-Laguna[1,2], A. Castro-Alvarez[3], M. Sledzinska[1], J. Maire[1], F. Costanzo[1], B. Ensing[1,5], M. Pruneda[1], P. Ordejón[1], C. M. Sotomayor Torres[1,4], P. Gómez-Romero[1] and E. Chávez-Ángel[1]

[1] Catalan Institute of Nanoscience and Nanotechnology (ICN2), CSIC and BIST, Campus UAB, Bellaterra, 08193 Barcelona, Spain

[2] Departament de Química, Universitat Autònoma de Barcelona, Cerdanyola del Vallès, 08193 Barcelona, Spain

[3] Organic Chemistry Section, Facultat de Química, Universitat de Barcelona, Av. Diagonal 645, 08028 Barcelona, Catalonia, Spain

[4] ICREA, Pg. Lluís Companys 23, 08010 Barcelona, Spain

[5] Van't Hoff Institute for Molecular Sciences, University of Amsterdam, 1098 XH Amsterdam, The Netherlands

E-mail: rocio.rodriguez@icn2.cat; emigdio.chavez@icn2.cat

Keywords: Nanofluids, Graphene, enhancement of thermal properties, π–π stacking, liquid layering, Raman of nanofluids, intermolecular forces.

Nomenclature

Abbreviations and Latin letters

BLS	Brillouin light scattering	*MD*	Molecular dynamics
Cp	Specific heat capacity at constant pressure (J/g K)	*n*	Refractive index of the medium
DFT	Density functional theory	*N-N*	Nitrogen-nitrogen
DLS	Dynamic light scattering	*NFs*	Nanofluids
DMAc	N,N-dimethylacetamide	*NMP*	N-Methyl-2-pyrrolidone
DMF	N,N-dimethylformamide	*NP*	Nanoparticles
DSC	Differential scanning calorimetry	*PCF*	Pair-correlation function
f	Brillouin frequency (Hz)	*TEM*	Transmission electron microscopy
HTFs	Heat transfer fluids	v_s	Sound velocity (m/s)
k	Thermal conductivity (W/m K)	*wt.* %	by weight (%)

Greek letters

λ_0	Laser wavelength (nm)	ν	Stretching (vibrational mode)
λ_s	Wavelength of the acoustic wave (nm)	3ω	Three-omega method

(*i*) Experimental methods

1. Sample preparation

Graphene flakes with lateral sizes ~ 150-450 nm and thicknesses from 1 to 10 layers were prepared from graphite (Sigma-Aldrich, purity > 99+% and size < 20 um) by a mechanical exfoliation method, similar to that used by Hermann et al.[61]. Thus, 0.4 g of graphite were ball-milled in a 100mL stainless steel jar with zirconia beads (5 and 12 mm diameter) in a high-energy planetary ball mill (All-direction planetary ball mill 0.4L, model CIT-XBM4X-V0.4L, Columbia International) at 378 rpm for 64 hours. From the resulting material, graphene nanofluids were prepared as follows. Graphene NFs were prepared based on DMAc (ACROS Organics, 99+ %) with concentrations ranging from 0.01-0.27 wt.% and DMF (Scharlau, HPLC grade) with concentrations ranging from 0.01-0.12 wt.%. Hereafter, for convenience, sample names will be shortened by omitting 'wt.% of graphene dispersed in', for example: 0.01 wt.% of graphene dispersed in DMAc will henceforth be written as 0.01 % DMAc. The preparation of the nanofluids consisted of direct mixing of the base fluid with graphene flakes. To suppress particle clustering and obtain stable dispersions[62], graphene was dispersed in the fluid using a high energy-planetary ball mill. Graphene and the solvent were mixed in a proportion of 1:31 in weight and were ball milled for 1 h, employing 5 and 12 mm diameter zirconia beads and 100 mL stainless steel jars. The ball to powder weight ratio used was 16:1 and the rotating speed of the jars was 378 rpm. Soft ultrasonic vibration, 1000 W (Ovan, model ATM40-6LCD) was then applied for 1h. After this procedure, the samples were centrifuged at 6000 rpm for one hour to ensure the stability of the nanofluids (Digicen 21 centrifuge, Orto alresa).

2. Dynamic light scattering

The stability of the graphene-based nanofluid dispersions was determined as a function of time using dynamic light scattering (DLS) system (ZetaSizer nano ZS, ZEN3600, Malvern Instruments, Ltd. Malvern). The samples were analysed periodically to register the number of photons scattered by the sample (one measurement per month). An attenuator index of 7 was applied to the laser and a quartz cuvette with a measurement position of 4.65 mm was used every time. The hydrodynamic diameter and the polydispersity index (PdI) of the sample were also obtained. Our measurements show that the total number of photons remained constant throughout the duration of the investigation. **Table S1** shows constant hydrodynamic diameter of the nanoflakes, photon count rate and PdI for a nanofluid based on DMAc during 4 months. The PdI describes how broad the size distribution is within the sample. Values range from 0.05-0.7, the smaller the PdI, the more monodisperse is a sample. Therefore, PdIs shown in Table S1 indicate that the sample is moderately monodisperse and together with the photon count rate values it can be said that there is no precipitation of graphene flakes throughout time.

Table S1 *DLS data from a graphene-nanofluid sample based on DMAc.*

Features / Time	**Day 1**	**After 2 months**	**After 3 months**	**After 4 months**
Hydrodynamic diameter (nm)	187 ± 9	184 ± 4	174 ± 6	179 ± 5
Photon count rate (kcps)	310 ± 2	334 ± 3	336 ± 2	333 ± 2
Polydispersity index	0.120 ± 0.031	0.111 ± 0.008	0.123 ± 0.018	0.102 ± 0.014

3. High-resolution transmission electron microscopy analysis

The dispersions were deposited on 300-mesh carbon grids, which were analyzed using the JEOL 1210 microscope, operating at 120 kV to obtain transmission electron microscopy (TEM) images. **Figure S1** shows a TEM image (*a*) of representative graphene flakes with different sizes (260-330 nm). The inset of **Figure S1*a*** shows selected area electron diffraction (SAED) from a graphene flake. As can be seen, single spots are obtained, which means a high crystallinity of the selected flake. Furthermore, the simulated SAED patter displayed in **Figure S1*b*** is in total accordance with the experiment, demonstrating the single crystal nature of the graphene flakes.

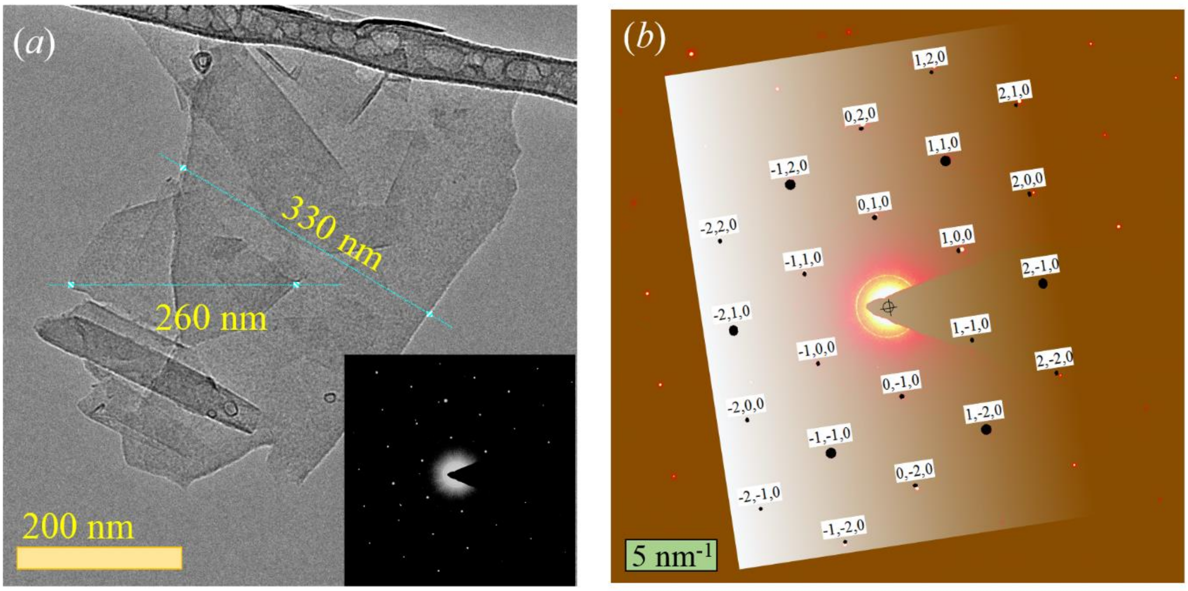

Figure S1 (*a*) *Representative TEM image of graphene from a DMAc dispersion (DMAc-NF) showing folded graphene sheets. (inset) Selected area electron diffraction (SAED) from the same graphene flake.* (*b*) *Simulated and experimental SAED pattern of multilayer graphene showing the different crystallographic planes.*

4. Brillouin Light Scattering

The sound velocities were determined from the Brillouin frequency shift measured for different graphene concentrations contained in a transparent quartz cuvette. A diode laser with wavelength λ_0 = 532 nm was focused with a 10x microscope objective, and the Brillouin spectra was recorded on JRS Tandem Fabry-Pérot TFP-1 interferometer in the backscattering configuration. The laser power was kept as low as possible (~ 2 mW) to avoid any possible heating effect from the laser.

Figure S2 displays the anti-stoke component of the Brillouin spectra for DMF and DMAc at different graphene concentrations. A small shift in the frequency as a function of graphene concentration is observed.

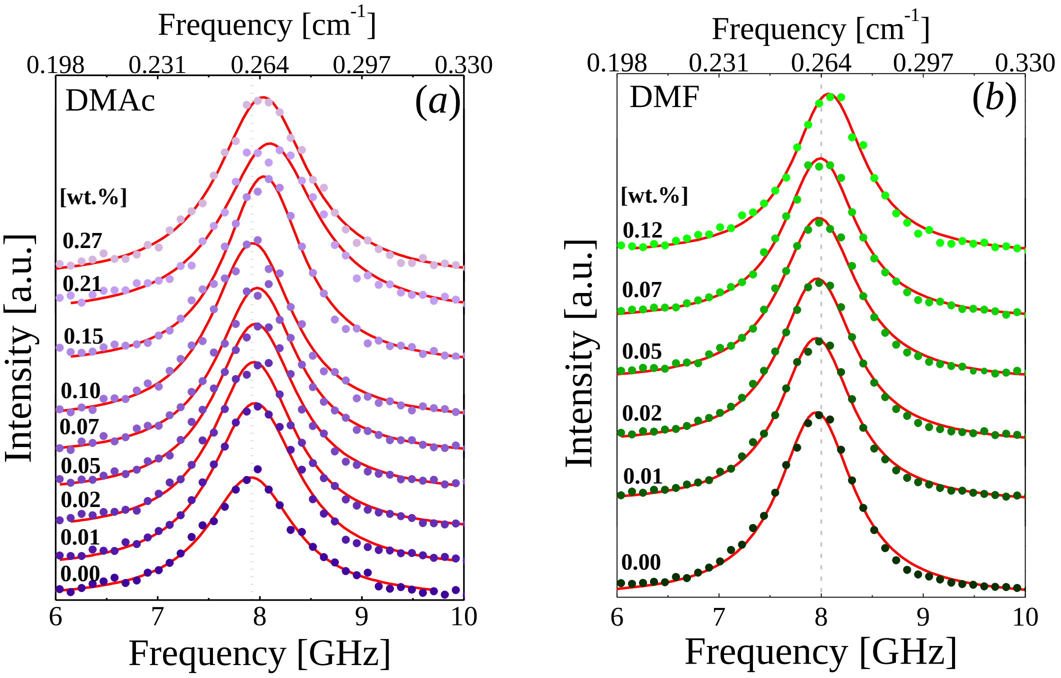

Figure S2 *Brillouin spectrum of DMAc (a) and DMF (b) NFs with different concentrations of graphene.*

5. Refractive index

The refractive index of the nanofluids were determined using the knife edge method.[3] This method consists of passing a laser light obliquely through a transparent container filled with the liquid to be measured. Due to the light passing through different media, the transmitted beam is displaced from its incident direction. This displacement depends on the refractive index of the liquid and the wall of the container. To eliminate the influence of the container wall, it is necessary to measure an empty cell and then, by subtracting the difference between both displacements, it is possible to estimate the refractive index of the liquid without reference to the refractive index of the container.[3]

A scheme of the set up used to measure the refractive index is illustrated in **Figure S3**. The measured refractive indices are displayed in the **Figure S4.** We can see that the refractive indices do not vary within of the experimental error bars.

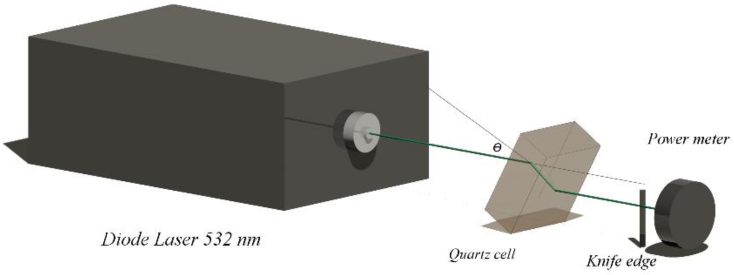

Figure S3 *Schematic representation that was used to measure the refractive index of the nanofluid.*

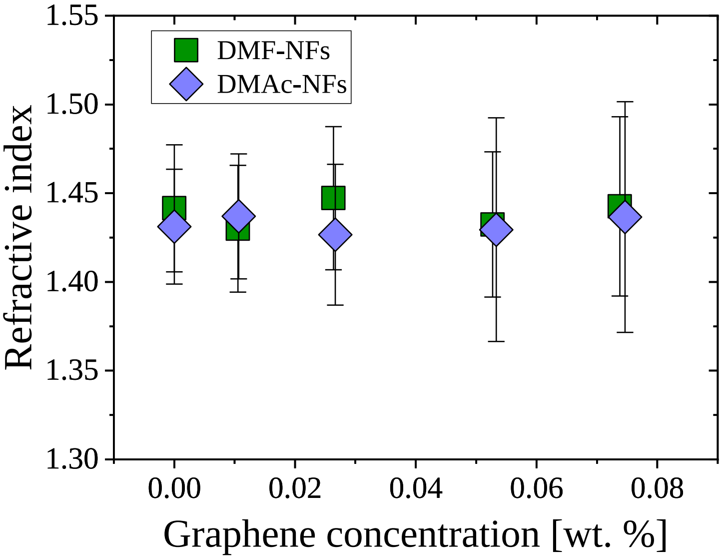

Figure S4 *Refractive index as a function of graphene concentration.*

6. Raman light scattering

The Raman spectra were recorded by T64000 Raman spectrometer manufactured by HORIBA Jobin Yvon. It was used in single grating mode with a spectral resolution better than 0.4 cm^{-1}. The liquid was placed in a transparent quartz cuvette, the same one used for Brillouin analysis. All the Raman measurements were carried out by focusing a diode laser (λ_0 = 532 nm) with 50x long working distance microscope objective. The power of the laser was kept as low as possible (~ 2 mW) to avoid any possible effect from self-heating.

The **Figure S5*a*** shows the Raman peak position of '$(CH_3)N$' rocking mode of pure DMF for several measurements. As can be seen, the reproducibility of the experimental setup varies in the order of 0.06 cm^{-1} (standard deviation, green parallel bar) within a range of 0.25 cm^{-1} (maximum and minimum peak deviation). It is important to mention that another possible factor that could produce a displacement of the Raman modes is the temperature fluctuation. To discard this effect, Raman measurements as a function of the laser power were performed. **Figure S5*b*** shows that the variation of the peak position of the "$(CH_3)N$" rocking mode of 0.5 mg/ml graphene-DMF is completely uncorrelated with the laser power. The range of variation was in ~ 0.24 cm^{-1} and with a standard deviation of 0.1 cm^{-1}, i.e., in the same range than the reproducibility of the equipment. Therefore, the displacements of the Raman band shown in this work are completely related to the strong interaction between graphene and DMF and cannot be associated with temperature fluctuation of the sample.

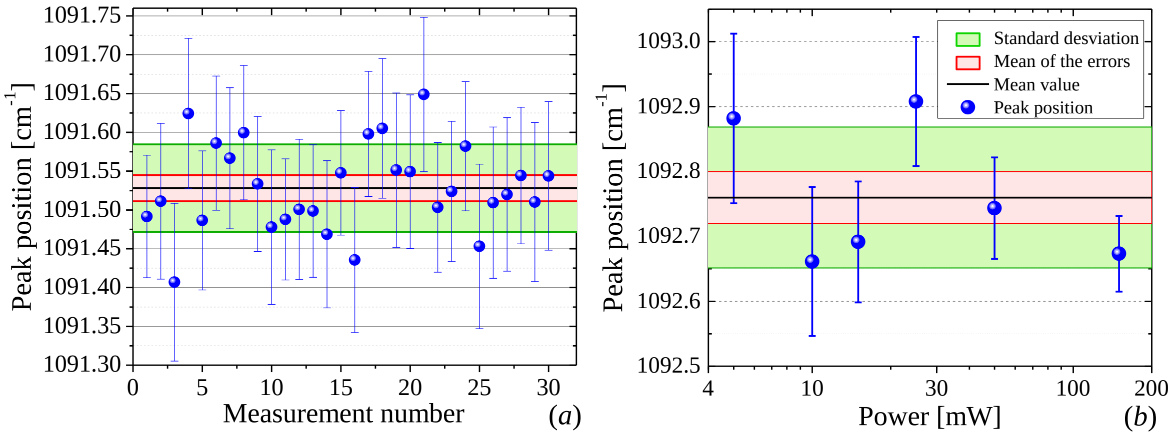

Figure S5 *Peak position of ~ 1091 cm^{-1} the rocking mode as function of: (a) measurement number (pure DMF) and (b) laser power (0.5 mg/m graphene-DMF nanofluid). The error bar of each measured point comes from the Lorentzian fit of the band. The average peak position is displayed in black solid line. The standard error of the averaged and mean errors are displayed with green and red parallel bars, respectively.*

The experimental Raman spectra from DMF-NFs at different graphene concentrations is plotted in **Figure S6**. This band corresponds to an asymmetric bending vibration in a plane (rocking) of the bond '$(CH_3)N$' of DMF molecule [5]. **Figure S6** shows a continuous displacement to higher frequencies and a broadening of the mode with increasing graphene concentration. The peak position was determined by a Lorentzian fit of the Raman spectra showed in solid red line.

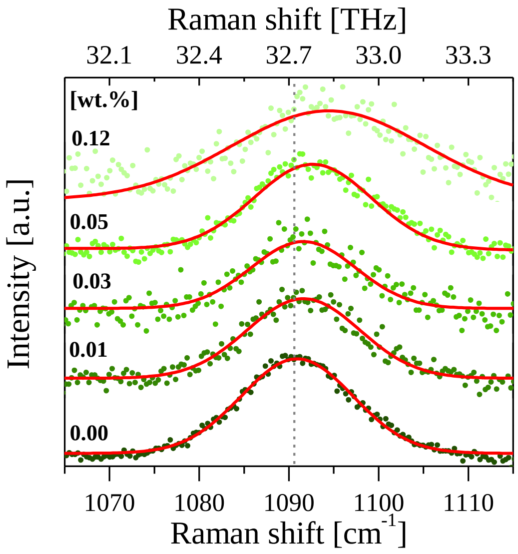

Figure S6 *Raman scattering from DMF NFs with different graphene flake concentrations: shift and broadening of the Raman spectra and the Lorentzian fit (solid red lines).*

7. Three-omega method

The three-omega (3ω) method is widely used to measure the thermal conductivity of solid materials[6,7]. In this work, we designed a modified version suitable for the measurement of liquids, based on the works of Chen et al.[8], Oh et al.[9] and Lubner et al.[10] Our cell is shown in **Figure S7**. The liquid is placed on the 3ω-heater which has been previously passivated with 200 nm of SiO_x, by plasma enhanced chemical vapor deposition, to avoid current leakage from the resistor to the conductive fluid. A 100 nm thick 3ω-strip (5 nm of chromium and 95 nm of gold) was patterned on a 0.5 mm thick quartz substrate by photolithography and electron beam physical vapor deposition (EBPVD). The width of the heating line is defined as $2b$ = 10 μm and the length as l = 1 mm, the latter considered as the distance between the voltage (inner) pads. Then, a 3 mm thick PDMS block is used to seal the circuit and to contain the liquid (as a well).

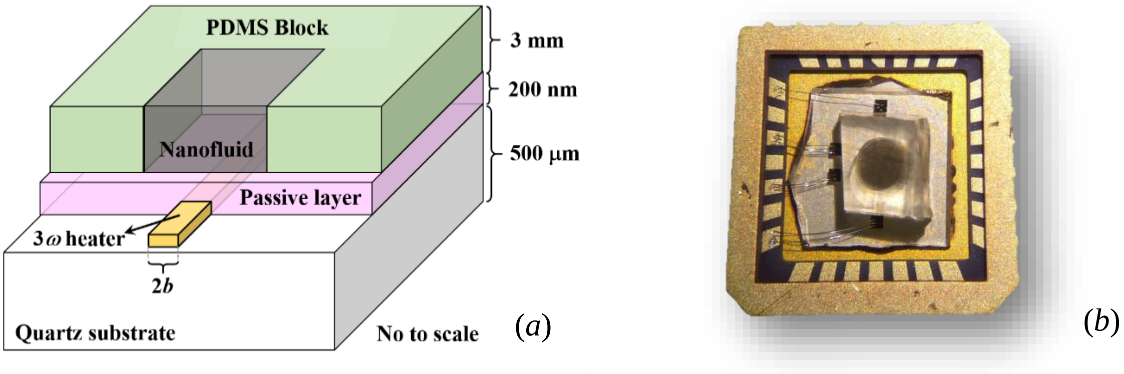

Figure S7 *3ω cell for fluid samples:* (*a*) *Schematic representation (b) Top view photograph of the actual cell containing a graphene nanofluid sample.*

The 3ω method consists of applying an alternating current (AC) through the metal strip which is in direct contact with the liquid. It is simultaneously a heater and thermometer. An AC signal with an angular frequency ω ($\omega = 2\pi f$, where f is the frequency) flows through the strip generating heat which oscillates at 2ω. The injected heat generates a temperature rise (ΔT) which will depend on the thermal properties of the sample. Since the electrical resistivity is linearly proportional to the temperature, see **Figure S8*a***, the ΔT can be obtained from this dependence. The temperature oscillations is obtained by measuring the third harmonic component of the voltage ($U_{3\omega}$) across the resistor using [6,7]:

$$\Delta T = \frac{2U_{3\omega}}{\beta U_0} \approx 2\frac{U_{3\omega,rms}}{\beta U_{\omega,rms}} \tag{1}$$

where U_0 is the voltage amplitude and β is the temperature coefficient of the electrical resistivity of the strip. Since the first harmonic amplitude is at least three order of magnitude larger than the third harmonic amplitude, one can approximate U_0 with U_ω. Finally, the thermal conductivity of the samples can be obtained by measuring the frequency dependence of the $U_{3\omega}$. The 3ω signal was recorded by 7260 DSP lock-in amplifier (EG&G Instruments) using a passive circuit.

The thermal conductivity of the substrate of an empty cell can be obtained by solving the transient heat conduction equation for a finite width line heater, deposited on the semi-infinite surface of a film-on-substrate system. The temperature rise is given by [6,7]:

$$\Delta T = \frac{P_l}{k\pi}\int_0^\infty \frac{\sin^2(xb)}{(xb)^2\sqrt{x^2+q^2}}dx = \frac{P_l}{k\pi}F(qb) \qquad (2)$$

where b is half heater width, $q \equiv 1/\lambda = \sqrt{2i\omega/\alpha}$ is the inverse of the thermal penetration depth (λ) α and k are the thermal diffusivity and conductivity of the substrate, respectively, and P_l is the AC power per unit length, i.e., P/l where l is the heater length.

7.1 Thermal conductivity determination of liquids

For the thermal conductivity determination of the liquid, the 3ω-strip was considered to be in the middle of the two semi-infinite media S (for substrate) and NF (for nanofluid). Then, assuming that the heat transfer occurs only across the interface liquid-heater-substrate, as in the boundary mismatch approximation, the total measured temperature oscillation of the heater (ΔT_{total}), including the substrate on one side and the nanofluid on the other, can be expressed as [8,9]:

$$\frac{1}{\Delta T_{total}} = \frac{1}{\Delta T_S} + \frac{1}{\Delta T_{NF}} \qquad (3)$$

where ΔT_S is the temperature rise of the substrate (measured in an empty cell) and the ΔT_{NF} is the temperature rise in the fluid. Lubner et al.[10] showed that the error using this approach is less than 1% at low-frequency limit (hundreds of Hz) when the ratio of the thermal diffusivities of the NF and S $\alpha_{NF}/\alpha_S > 10^{-1}$ (in our case $\alpha_{NF}/\alpha_S > 0.2$) and the thermal conductivities ratio $10^{-2} < k_{NF}/k_S < 1$ (in our case $k_{NF}/k_S < 0.22$). Finally, the thermal conductivity of the fluid can be estimated by solving Eq. (2) using least squares fit.

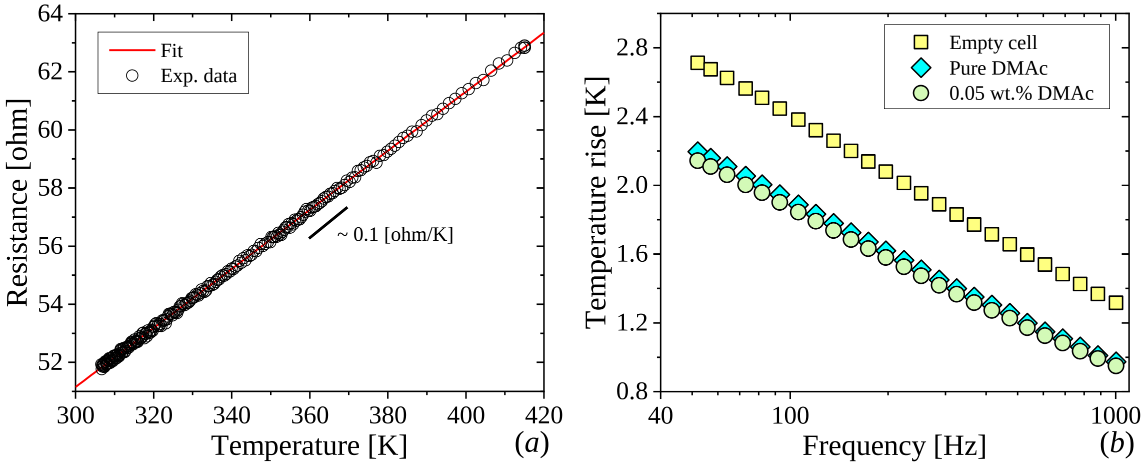

Figure S8 (*a*) *Electrical resistance against temperature of 3ω strip.* (*b*) *Typical temperature rise as a function of the frequency showing: empty cell (yellow solid squares) and filled cell with DMAc (blue solid diamonds) and 0.05 wt% graphene-DMAc (green solid circles).*

A summary of the thermal conductivity data in this work is shown in **Table S2** and **Table S3**. The measured values of the thermal conductivity were corrected using a factor to allow the comparison of data from different 3ω cells. The measurement of *k* of DMAc NFs was performed using different 3ω cells, on the other hand, a single 3ω cell was used to measure the whole set of concentrations of DMF-NFs. The bare fluids were used as standards and analyzed in order to corroborate the proper operation of each cell. The thermal conductivity of our samples was corrected by a factor, obtained from the bare fluids measurements. Previous to the measurement of each sample, the thermal conductivity of the bare fluid is measured and compared with the well-accepted value from the literature. Then a correction factor is obtained and the thermal conductivity of the bare fluid is corrected. After that the *k* of NF is measured and corrected by the same factor. In order to check the reproducibility of the measurement, at least four measurements for each sample were repeated with a standard deviation smaller than 0.01 W/m K .

The experimental thermal conductivity values of the base fluids are in broad agreement with the widely accepted values of *k* = 0.17 W/m K and 0.18 W/m K for DMAc and DMF, respectively [11].

Table S2 *Thermal conductivity data from graphene-DMAc nanofluids at 298 K.*

Concentration wt.%	***k* (W/mK)**	**Correction factor**	**corrected *k* (W/mK)**	***k* enhancement (%)**
0.00	0.184±0.001	0.95	0.175±0.001	0±0.8
0.01	0.191±0.001	0.94	0.180±0.001	2.6±0.8
0.03	0.168±0.001	1.17	0.196±0.001	11.9±0.8
0.05	0.174±0.001	1.18	0.206±0.001	17.7±0.8
0.18	0.281±0.003	0.92	0.259±0.003	47.9±1.2

Table S3 *Thermal conductivity data from graphene-DMF nanofluids at 298 K.*

Concentration wt.%	*k* (W/mK)	Correction factor	corrected *k* (W/mK)	*k* enhancement (%)
0.00	0.172±0.001	1.06	0.183±0.001	0.0±0.8
0.01	0.183±0.002	1.06	0.194±0.002	6.0±1.0
0.03	0.191±0.001	1.06	0.203±0.001	11.1±0.8
0.05	0.215±0.001	1.06	0.228±0.001	24.6±0.8

8. Differential scanning calorimetry

Specific heat capacity (Cp) was measured by using differential scanning calorimetry (DSC) on a PerkinElmer DSC 8000, using a common procedure. The difference in heat flow between an empty pan (standard aluminum pan) and the sample (inside the same pan) is recorded as a function of temperature; both measurements are taken using the same thermal program, heating rate and temperature range. In particular, the conditions used in this work are described as follows: from 5-20ºC at 2ºC/min, adding two 10-minutes isotherms at the beginning and at end of the measurement. Platinum was used as a standard and analyzed by DSC in order to corroborate the proper operation of the equipment. The specific heat capacity of our samples was corrected by a factor of 1.13, obtained from the Pt measurements, in accordance with the standard procedure for DSC analysis.

Table S4 shows a summary of the results and the corresponding *Cp* enhancement of the NFs. The results obtained for the base fluids are in good agreement with the values found in the literature: 2.06 J/gK and 2.016 J/gK for DMF and DMAc, respectively, at 298 K [11].

Table S4 *Specific heat capacity data from graphene-DMAc and DMF nanofluids at 293K.*

Concentration wt.%	DMAc		DMF	
	Corrected *Cp* (J/gK)	*Cp* enhancement (%)	Corrected *Cp* (J/gK)	*Cp* enhancement (%)
0.00	2.05±0.02	0.00	2.07±0.02	0.00
0.01	2.15±0.02	4.89±1.45	--	--
0.03	--	--	2.13±0.02	2.83±1.44
0.05	2.16±0.02	5.11±1.45	2.22±0.02	7.23±1.47
0.11-0.12	2.41±0.02	17.71±1.56	2.32±0.02	12.07±1.51

It is important to remark that, as the enhancement of *Cp* is not as large as for *k* (see **Table S2** and **Table S3**), the overall thermal diffusivity ($\alpha = k/(\rho\, Cp)$, with ρ being the material density) of NFs will also increase as a function of graphene concentration. For example, taking the experimental *k* and *Cp* data for 0.05 wt.% graphene-DMAc NF, the thermal diffusivity enhancement is $\alpha \sim 12$ %. This result demonstrates the potential of these NFs as heat transfer fluid for cooling applications.

9. Effective viscosity measurements

The effective viscosity of the nanofluids was measured using a Haake RheoStress RS600 rheometer from Thermo Electron Corp. at T = 20-21ºC. The shear rate used was 2880 s^{-1} with a measurement time of 30 seconds.

Figure S9 displays the viscosity of the nanofluids as a function of graphene concentration at room temperature. The viscosity of both sets of graphene nanofluids increases considerably as a function of graphene concentration. DMAc nanofluids with low graphene loading (0.00-0.03 wt. %) have similar viscosity values.

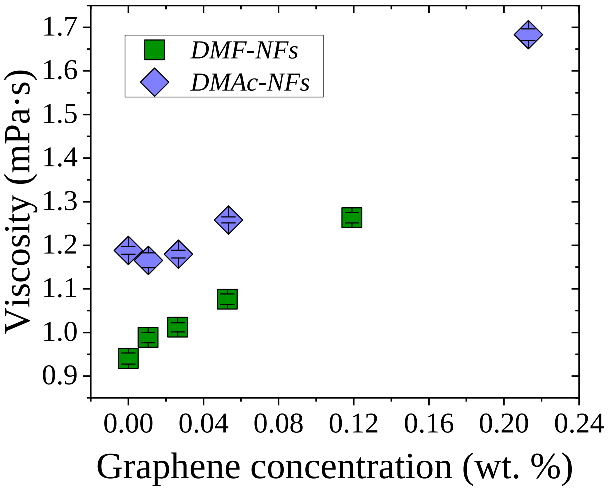

Figure S9 *Viscosity of graphene-DMAc and DMF nanofluids as a function of graphene concentration.*

(*ii*) Theoretical modelling

1. Molecular dynamics and DFT calculations: procedure

A combination of density functional theory (DFT) and molecular dynamic (MD) simulations was used to calculate the most frequent DMF-graphene configurations (DMF molecules orientation to graphene) and their respective Raman frequencies. Geometry optimization, energies and Raman modes were calculated using DFT methods (B3LYP). The DMF-graphene configurations were obtained from MD simulations, using a OPLS-2005 [12,13] classical force field. Then, singlet-point calculations were carried out at a higher DFT level (ωB97XD). The methodology used in this work is summarized in **Figure S10.**

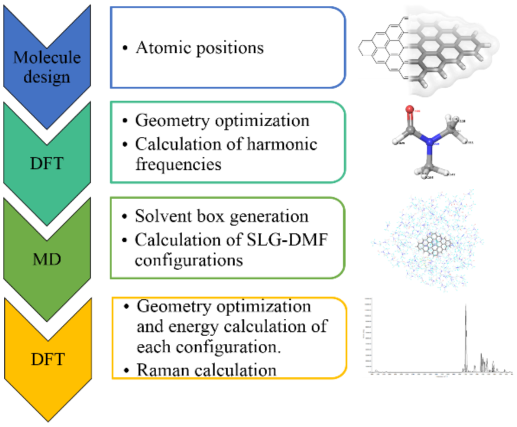

Figure S10 *Flow diagram of the method used.*

2. Molecule design and first DFT optimization

Initially, a 4x4 unit cell for SLG and a single DMF molecule were generated using the Avogadro software [14] (see **Figure S11**). The resulting structures were optimized with the Becke's three-parameter exchange (B3) + Lee-Yang-Parr (LYP) correlation functional (B3LYP) [15–18] using Pople 6-31G(d)[19] basis set. The calculations were done with Gaussian 09 [20]. The map of electrostatic potential (ESP) [21,22] allowed to calculate the partial atomic charge distributions of the molecules, which were used as point charges in the OPLS force field. Once the energy was minimized, the harmonic frequencies were calculated to corroborate the energy minimization. Our compute frequencies are corrected by a scaling factor [23] of 0.961.

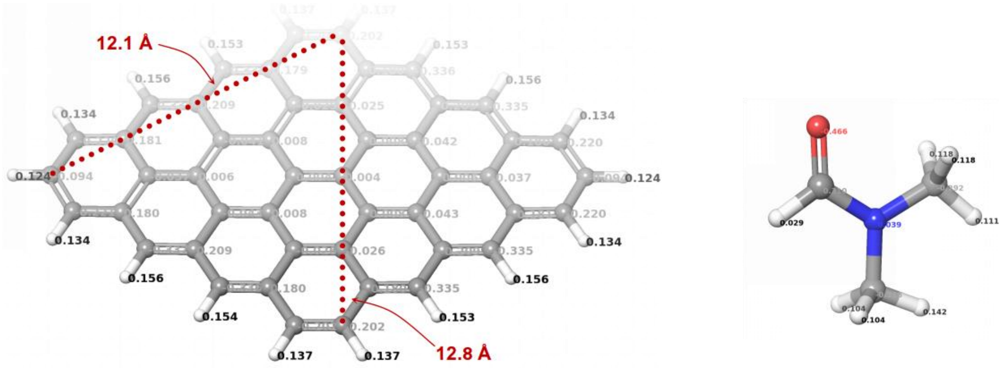

Figure S11 *Molecular geometries and partial charges of the graphene flake (left) and DMF molecule (right). The partial charges were those calculated with B3LYP/6-31G(d).*

3. Molecular dynamics simulations

Starting with the optimized DMF molecule, we generated a cubic solvent box for the MD simulations. For this purpose, the Disordered System Builder module of the Schrödinger material suite [24] was used to create a multicomponent system of randomly distributed molecules of DMF consisting of 512 molecules with a van der Waals scalar factor of 0.80. The system was optimized for a period of 200 ps; the ESP partial charges were those calculated by B3LYP/6-31G(d). Once this model was generated, the equilibration of the complete system (SLG+DMFs) was performed for 100 ps at T = 300 K and constant volume. This was followed by MD simulations for 100 ns maintaining a cubic solvation model at constant temperature and pressure of 1.013 bars. A schematic representation of the calculation is shown in the

Figure S12**.**

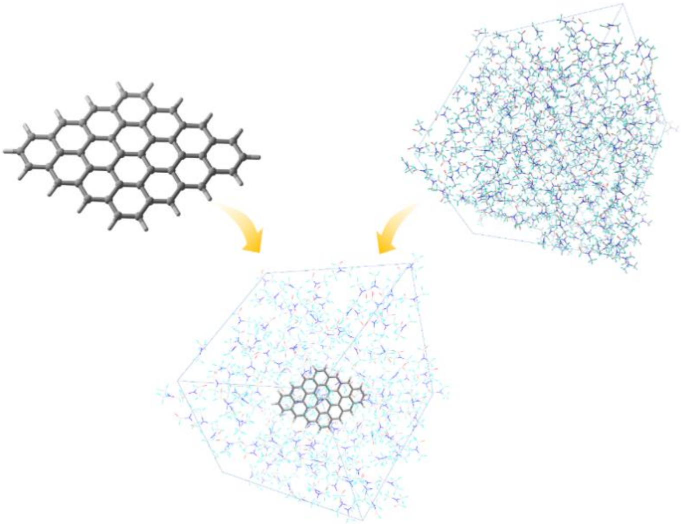

Figure S12 *Schematic representation of the studied system: graphene surrounded by 512 DMF molecules.*

The data from 100 ns long MD simulations were performed using scripts written in Python. Firstly, the trajectory of the system was divided into 1000 frames, i.e., we have an image of the whole system every 0.1 ns. These frames were analyzed identifying ten configurations containing two or three molecules of DMF with different orientations (with respect to graphene) were identified as the most frequent ones. Three different SLG-DMF configurations, identified as **A**, **B** and **C** (see **Figure S13**), were found with the highest occurrence of 59.7%, 17.6% and 8.1%, respectively. The rest of configurations showed an occurrence below 5% and 1% (see red and blue regions depicted in **Figure S14**).

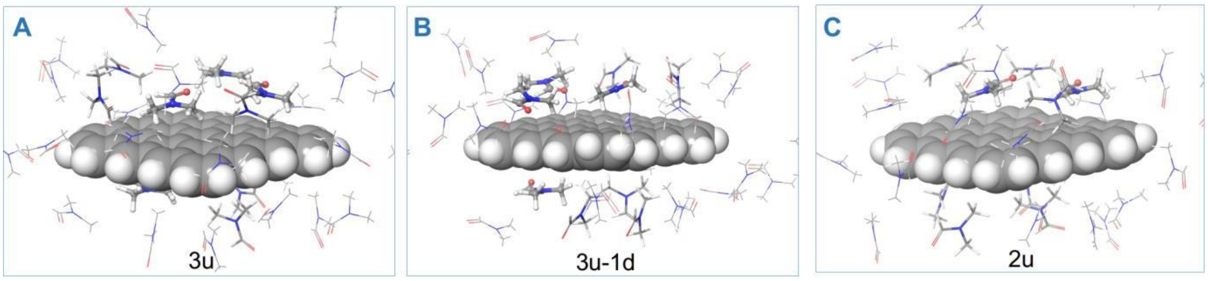

Figure S13 *The three different SLG-DMF configurations with the highest occurrence: A (59.7%), B (17.6%) and C (8.1%).*

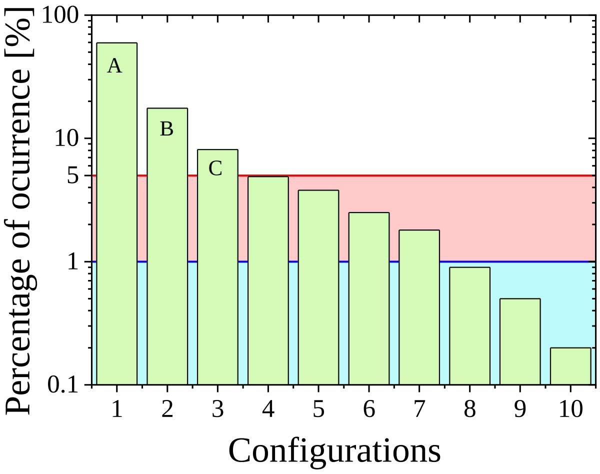

Figure S14 *Percentage of occurrence of the different identified configurations.*

A snapshot of SLG and some DMF molecules around of it is displayed in **Figure S15**. The natural formation of the hydrogens bonds with distances ~ 2.6-3.0 Å are shown with pink dotted lines.

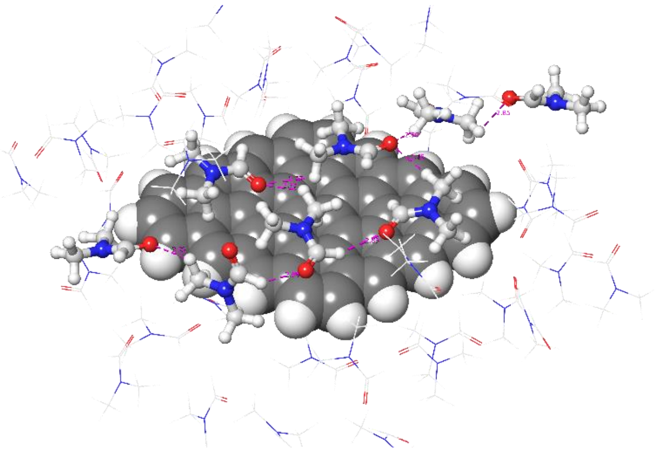

Figure S15 *Representative snapshot of the MD simulation showing the natural formation of hydrogen bonds among DMF molecules.*

4. DFT energy calculation, second geometry optimization and Raman modes

4.1 Energy calculation of MD configurations

The energy calculations of SLG-DMF systems were carried out for each configuration using the hybrid functional B3LYP, including London dispersion corrections suggested by Grimme [25]. This correction helps in the distribution of charges in hydrocarbon molecules and in molecules where inter and intramolecular van der Waals interactions are very important, as in the case of graphene structures. The ωB97X-D3 functional [26,27] with the 6-311+G(d,p) basis set was also used.

Configuration **A** turned out to be the most energetically favorable system, containing three DMF molecules that were oriented in parallel to the SLG. Configuration **B** presented a similar configuration to **A** but with an extra DMF molecule located under graphene, also with a parallel orientation. This extra molecule produces an energy imbalance of the system of 5.2 kcal/mol as compared to **A**, as shown in **Figure S16**. Configuration **C** is the simpler system, which contains 2 molecules of DMF in a parallel orientation located in the center of SLG and was found 7.3 kcal/mol above **A**.

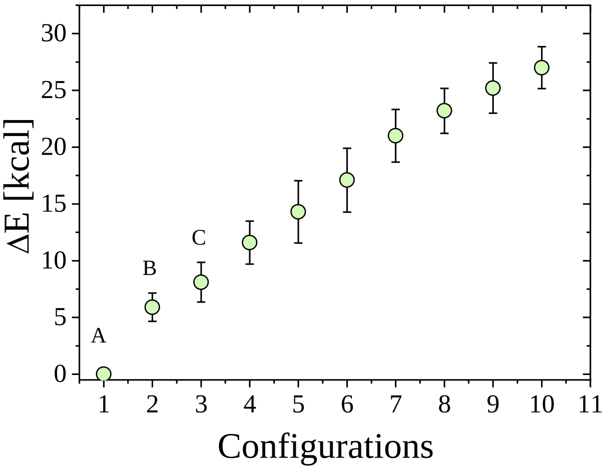

Figure S16 *DFT energy difference between the most energetic favorable SLG-DMF configurations (A) and the remaining two configurations.*

4.2 Molecular orbitals and non-covalent interactions (NCI)

To better understand the nature of SLG-DMFs interaction, we examined the electronic properties of the bound states. The highest occupied molecular orbital (HOMO) and the lowest unoccupied molecular orbitals (LUMO) of SLG-DMFs systems (**A**, **B** and **C**) are shown in **Figure S17**. The HOMO-LUMO gap is similar for the three studied configurations. Both the LUMO and the HOMO, HOMO-1 and HOMO-2 orbitals are mainly located in the SLG, which defines the gap of the system. The HOMO-3 shows the best delocalization of the electronic density, being a mixture of DMF and SLF states. On the DMF molecule, it is located mainly on the nitrogen and oxygen (where the available p orbitals for π-π interactions), and delocalized over the entire SLG. As expected, the electronic density is concentrated on the amide group due to the delocalization of the nitrogen electron pair onto the C=O group. Configuration **A** clearly shows the highest electron density in comparison with the other configurations. In all the cases, the gap between the sub-level HOMO-3, and its corresponding LUMO is ~0.22 eV. In other words, the parallel geometry of the DMF molecules in respect to SLG favors the formation of a molecular orbital, with participation of the DMF p-orbitals (HOMO-3), and delocalized π states of graphene.

Another method to evaluate non-covalent interactions (NCIs) is based on the analysis of reduced density gradient [28,29]. We analyzed the electron densities and their reduced gradients obtained in the DFT calculations, for the three configurations (**A**, **B** and **C**) using NCIPlot[30]. This method enables the identification of NCIs by plotting the isosurfaces of the reduced density gradient in the real space. This approach allows to distinguish a wide range of binding energies, encompassing strong and weak (attractive and repulsive) intermolecular interactions such as: CH-π and π-π, van der Waals, hydrogen and halogen bonds, etc. As is shown in **Figure S18**, weak interactions are present in all the SLG-DMF configurations. However, the configuration A shows the largest interaction area in relation with the other configurations.

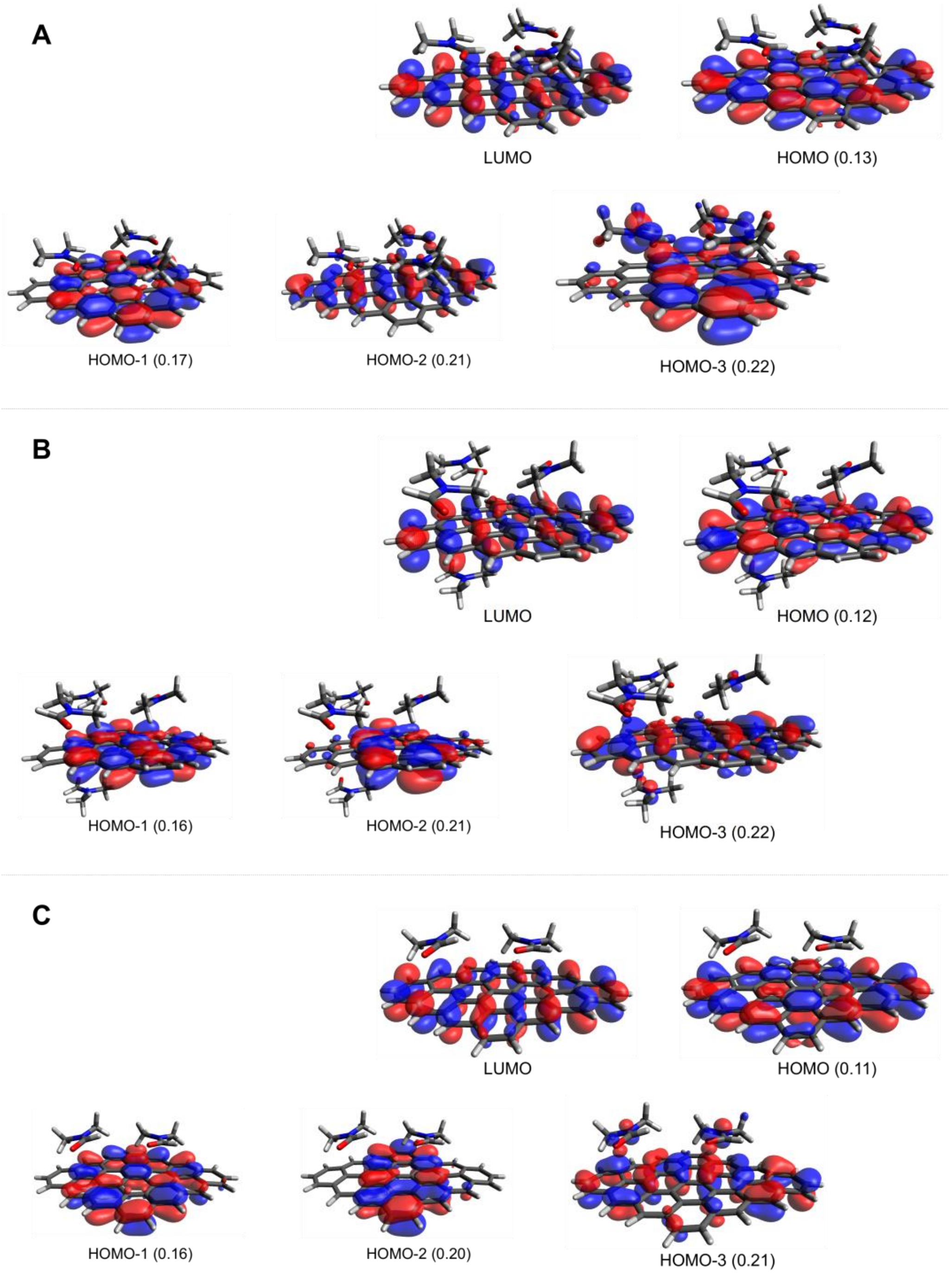

Figure S17 *HOMO and LUMO orbitals of the **A**, **B** and **C** configurations. The number in parentheses are the energy differences between the corresponding frontier orbitals. The red and blue clouds represent the regions positive and negative values of the wavefunctions, respectively.*

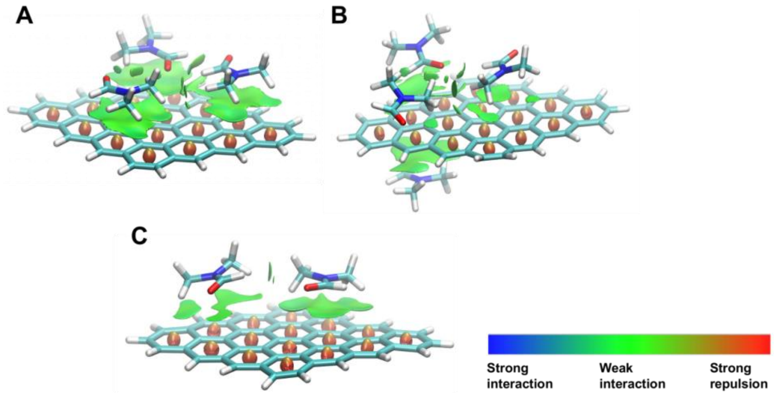

Figure S18 *Analysis of non-covalent interactions of the three studied configurations.*

4.3 Raman calculation

The Raman frequencies were calculated at gamma point for the three optimized configurations. We used two different functionals B3LYP and ωB97X-D3 with 6-311+G(d, p) as the basis set. The calculations also included the dispersion correction suggested by Grimme [25]. **Table S5** shows the comparison between the experimental Raman peaks of pure DMF and 0.05 wt% NF and the theoretical results. We identified two Raman modes as: rocking (1091 cm^{-1}) and stretching (1438 cm^{-1}). It can be seen that both the experimental data and the theoretical modelling of the Raman peaks are blue shifted in respect to the pure DMF.

Table S5 *Calculated Raman frequencies for the SGL–DMF configurations using B3LYP-D/6-311+G (p,d) and ωB97X-D3/6-311+G (p,d).*

Experimental frequencies (cm^{-1})		**Theoretical frequencies (cm^{-1})**							
		B3LYP-D/6-311+G(d,p)				**ωB97X-D3/6-311+G(d,p)**			
DMF	0.05 wt.%	DMF	A	B	C	DMF	A	B	C
1090.9	1092.6	1092.9	1096.3	1113.0	1094.2	1103.0	1108.5	1110.1	1111.5
1438.5	1439.8	1430.7	1443.7	1442.5	1440.3	1452.0	1448.2	1458.0	1454.0

4.4 Height dependent radial distribution of DMF

To investigate the formation of layering and increased order in the DMF solvent interacting with the SLG flake, we computed the nitrogen-nitrogen pair-correlation function of DMF as a function of the height above (or below) the SLG from a 10 ns NPT simulation of a single flake in DMF. Here, a disk-like SLG of 348 carbon atoms was built with the Avogadro software, positioned in a cubic box with its normal vector along the z-axis, and dissolved in 4350 DMF molecules using the Packmol software [31]. The NPT (constant temperature and pressure) simulation was performed with the LAMMPS [32] program using the fully flexible OPLS-AA force field [33], after energy minimizing and performing 100 ps runs for (*i*) isochoric warming up, (*ii*) NVT (constant temperature and volume) equilibration, and (*iii*) NPT equilibration. The RESPA multi-time step algorithm [34] was used with an outer time step of 1 fs. The temperature was controlled at T =300 K by a CSVR thermostat [35] with a period of 0.1 ps, while a Parrinello-Rahman barostat [36] set to p =1 atm was employed with a period of 1 ps. In each stage of these simulations, the SLG was constrained to remain with its normal vector along the z-axis by removing every MD step any total angular velocity from the SLG.

The height dependent pair-correlation function (or radial distribution function) was obtained by computing over the 10 ns trajectory (1 ps frame interval) the relative density of nitrogen atoms around a central nitrogen atom as a function of its distance in a 2D slab with thickness $\boldsymbol{dz}$. Note that, at variance with the usual radial distribution, which quantifies the relative density on a 3D sphere ($g(\boldsymbol{r})= 4\pi r^2 \rho d\boldsymbol{r}$), here we obtain the density on the surface of a cylinder with height $\boldsymbol{dz}$ ($g(\boldsymbol{r})= 2\pi \boldsymbol{r} \rho d\boldsymbol{r} d\boldsymbol{z}$), centered at the central nitrogen atom. In the loop over central nitrogen atoms, only atoms were selected that were within 4 Å of the main axis of the 33-Å diameter SLG, and their $\boldsymbol{z}$-height above (or below) the flake was histogrammed with a bin size of $\boldsymbol{dz}$. The radial bin size, $\boldsymbol{dr}$, was set to 0.1 Å and $\boldsymbol{dz}$ was set to 1.0 Å. For convenience we will rename the coordinates as: $\boldsymbol{z}$ = x-axis and $\boldsymbol{r}$ = y-axis following the axis nomenclature of the **Figure S19*a***.

Figure S19*a* shows three dimensional color map of nitrogen-nitrogen (N-N) pair as function of graphene distance (x-axis) and N-N pair distance (y-axis). Far from the flake, at $x \approx \pm$ 29.5 Å, is seen a high density centered at $y \approx$ 6.0 Å as is shown green solid lines of **Figure S19*b***, i.e., the typical liquid behavior. Where the contribution of the first coordination shell is always higher than non-existing second, third shells, etc. due the non-long range order in a liquid. However, near the flake at $x \sim \pm$3.45 Å three well defined peaks are seen at N-N distance $y \approx$ 6.5, 11.6 and 16.5 Å, corresponding to first, second and third coordination shells, respectively (see black solid line in **Figure S19*b***). These results show a strongly ordered (although still liquid) structure of the DMF molecules close to the graphene.

Figure S19*b* shows that the first peak at $x \approx$ 3.45 Å is shifted ~ 0.5 Å in respect with the analogous peak at higher distances from the graphene flake. This can be explained in terms of the preferential orientation of the DMF molecules. Further from graphene there is not a preferential orientation of DMF molecules, but close to graphene they tend to lay parallel to the flake, requiring a larger N-N distance in the first coordination shell.

Figure S19*c* shows an interesting behavior of the liquid as a function of graphene distance (x), as can be seen the plot shows an oscillatory trend of the N-N correlation function as a function of graphene distance. The minimum and maximum profile in the x-direction, reveal that there is a short range structuring of DMF molecules extending to ~ 20 Å out from the flake. Certainly, three DMF layers can be distinguished, reaching at least 15 Å from the flake. The maximum height of the peaks can be seen at a distance of $x \approx$ 3.45 Å (black solid line in **Figure S19*b*** and grey dotted line in **Figure S19*c***) and followed by a minimal density at $x \approx$ 6.2 Å from the flake (see grey dotted line in **Figure S19*b*** and first dip of **Figure S19*c***), which separates the first DMF layer from the second. Therefore, graphene is affecting not only the ‘layer’ of DMF molecules which is in direct contact with the flake but the second and third layers. The effect is lost thereafter. In the y direction, the DMF structuring ranges at least 18

Å, which is remarkable considering that the flake radius is only 16.5 Å; hence, on larger flakes even longer-ranged ordering may be expected.

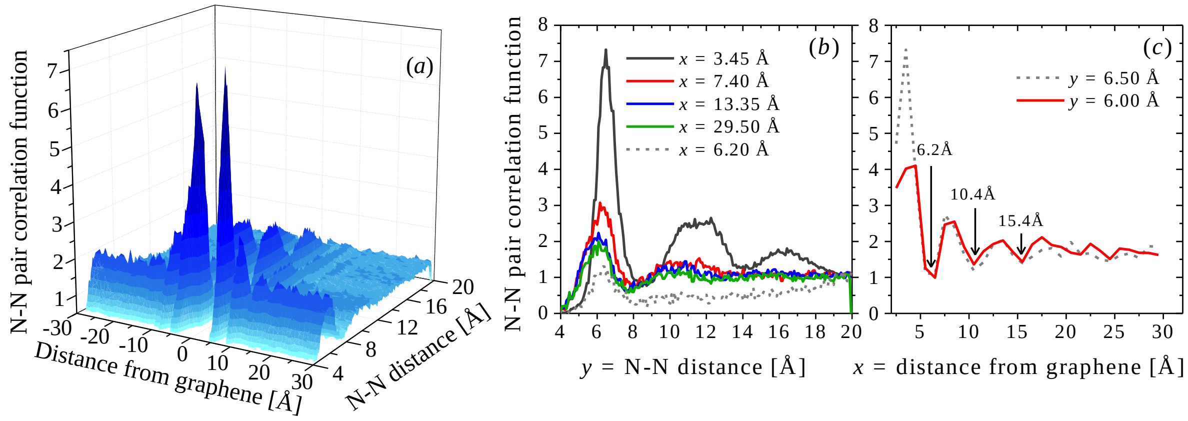

Figure S19 (*a*) *Three dimensional (3D) color map of nitrogen-nitrogen pair correlation function (z-axis) as function of graphene distance (x-axis) and N-N distance (y-axis).* (*b*) *Five vertical cuts of the 3D color map at different distances of the graphene flake (x) in the zy-plane.* (*c*) *Two vertical xz-plane cuts centered at different N-N distances (y).*

References

1 H. Hermann, T. Schubert, W. Gruner and N. Mattern, *Nanostructured Mater.*, 1997, **8**, 215–229.

2 V. Trisaksri and S. Wongwises, 2007, **11**, 512–523.

3 S. Nemoto, *Appl. Opt.*, 1992, **31**, 6690.

4 T. M. Aminabhavi and B. Gopalakrishna, *J. Chem. Eng. Data*, 1995, **40**, 856–861.

5 V. Venkata Chalapathi and K. Venkata Ramiah, *Proc. Indian Acad. Sci. - Sect. A*, 1968, **68**, 109–122.

6 D. G. Cahill, *Rev. Sci. Instrum.*, 1990, **61**, 802–808.

7 D. G. Cahill, *Rev. Sci. Instrum.*, 2002, **73**, 3701.

8 F. Chen, J. Shulman, Y. Xue, C. W. Chu and G. S. Nolas, *Rev. Sci. Instrum.*, 2004, **75**, 4578–4584.

9 D.-W. Oh, A. Jain, J. K. Eaton, K. E. Goodson and J. S. Lee, *Int. J. Heat Fluid Flow*, 2008, **29**, 1456–1461.

10 S. D. Lubner, J. Choi, G. Wehmeyer, B. Waag, V. Mishra, H. Natesan, J. C. Bischof and C. Dames, *Rev. Sci. Instrum.*, , DOI:10.1063/1.4905680.

11 D. R. Lide, *CRC Handbook of Chemistry and Physics*, Boca Raton, FL, CRC Press., 2005.

12 J. L. Banks, H. S. Beard, Y. Cao, A. E. Cho, W. Damm, R. Farid, A. K. Felts, T. A. Halgren, D. T. Mainz, J. R. Maple, R. Murphy, D. M. Philipp, M. P. Repasky, L. Y. Zhang, B. J. Berne, R. A. Friesner, E. Gallicchio and R. M. Levy, *J. Comput. Chem.*, 2005, **26**, 1752–1780.

13 G. A. Kaminski, R. A. Friesner, J. Tirado-Rives and W. L. Jorgensen, *J. Phys. Chem. B*, 2001, **105**, 6474–6487.

14 M. D. Hanwell, D. E. Curtis, D. C. Lonie, T. Vandermeersch, E. Zurek and G. R. Hutchison, *J. Cheminform.*, 2012, **4**, 17.

15 S. H. Vosko, L. Wilk and M. Nusair, *Can. J. Phys.*, 1980, **58**, 1200–1211.

16 C. Lee, W. Yang and R. G. Parr, *Phys. Rev. B*, 1988, **37**, 785–789.

17 A. D. Becke, *J. Chem. Phys.*, 1993, **98**, 5648–5652.

18 P. J. Stephens, F. J. Devlin, C. F. Chabalowski and M. J. Frisch, *J. Phys. Chem.*, 1994, **98**, 11623–11627.

19 R. Ditchfield, W. J. Hehre and J. A. Pople, *J. Chem. Phys.*, 1971, **54**, 724–728.

20 M. J. Frisch, G. W. Trucks, H. B. Schlegel, G. E. Scuseria, M. A. Robb, J. R. Cheeseman, G. Scalmani, V. Barone, B. Mennucci, G. A. Petersson, H. Nakatsuji, M. Caricato, X. Li, H. P. Hratchian, A. F. Izmaylov, J. Bloino, G. Zheng, J. Sonnenb and D. J. Fox, 2009.

21 U. C. Singh and P. A. Kollman, *J. Comput. Chem.*, 1984, **5**, 129–145.

22 B. H. Besler, K. M. Merz and P. A. Kollman, *J. Comput. Chem.*, 1990, **11**, 431–439.

23 J. P. Merrick, D. Moran and L. Radom, *J. Phys. Chem. A*, 2007, **111**, 11683–11700.

24 2017.

25 S. Grimme, *Wiley Interdiscip. Rev. Comput. Mol. Sci.*, 2011, **1**, 211–228.

26 J.-D. Chai and M. Head-Gordon, *Phys. Chem. Chem. Phys.*, 2008, **10**, 6615.

27 J.-D. Chai and M. Head-Gordon, *J. Chem. Phys.*, 2008, **128**, 84106.

28 E. R. Johnson, S. Keinan, P. Mori-Sánchez, J. Contreras-García, A. J. Cohen and W. Yang, *J. Am. Chem. Soc.*, 2010, **132**, 6498–6506.

29 G. Saleh, C. Gatti and L. Lo Presti, *Comput. Theor. Chem.*, 2012, **998**, 148–163.

30 J. Contreras-García, E. R. Johnson, S. Keinan, R. Chaudret, J.-P. Piquemal, D. N. Beratan and W. Yang, *J. Chem. Theory Comput.*, 2011, **7**, 625–632.

31 L. Martínez, R. Andrade, E. G. Birgin and J. M. Martínez, *J. Comput. Chem.*, 2009, **30**, 2157–2164.

32 S. Plimpton, *J. Comput. Phys.*, 1995, **117**, 1–19.

33 W. L. Jorgensen and J. Tirado-Rives, *J. Am. Chem. Soc.*, 1988, **110**, 1657–1666.

34 M. Tuckerman, B. J. Berne and G. J. Martyna, *J. Chem. Phys.*, 1992, **97**, 1990–2001.

35 G. Bussi, D. Donadio and M. Parrinello, *J. Chem. Phys.*, 2007, **126**, 14101.

36 M. Parrinello and A. Rahman, *J. Appl. Phys.*, 1981, **52**, 7182–7190.